Electronic Supplementary Information

Elucidating and controlling phase integration factor in Co-free Li-rich layered cathode for lithium-ion batteries

Youngsu Lee[a], Jaesub Kwon[b], Jong-Heon Lim[a], Eunseong Choi[a], Kyoung Eun Lee[a], Shin Park[a], Docheon Ahn[c], Changshin Jo[a, d], Yong-Tae Kim[b], Yoon-Uk Heo[a], Geunho Choi[e], Byongyong Yu[e], Inchul Park[e, *], and Kyu-Young Park[a,b, *]

[a.] Graduate Institute of Ferrous & Eco Materials Technology, Pohang University of Science and Technology (POSTECH), Pohang 37673, Republic of Korea.

[b.] Department of Materials Science and Engineering, Pohang University of Science and Technology (POSTECH), Pohang 37673, Republic of Korea.

[c.] Beamline Department, Pohang Accelerator Laboratory, Pohang 790-784, Republic of Korea

[d.] Department of Chemical Engineering, Pohang University of Science and Technology (POSTECH), Pohang 37673, Republic of Korea.

[e.] Secondary Battery Materials Lab, POCSO N.EX.T Hub, POSCO Holdings, 100 Songdogwahak-ro, Yeonsu-gu, Incheon, 21985, Republic of Korea.

Submitted to

Materials Horizons

2025

* Corresponding authors.

E-mail: kypark0922@postech.ac.kr; phone: +82-54-279-9299

Table of contents

Experimental Sections

Synthesis

The $Ni_xMn_{1-x}(OH)_2$ (x=0.25, 0.35, 0.40) precursors and Li_2CO_3 precursor were provided by an industrial partner. Each $Ni_xMn_{1-x}(OH)_2$ (x=0.25, 0.35, 0.40) was mixed with Li_2CO_3 according to the target composition ratios. For the stoichiometric compositions, the Li/TM precursor ratios were set at 1.5:1, 1.3:1, and 1.2:1, respectively. For the off-stoichiometric compositions, the Li/TM precursor ratios were adjusted to 1.58:1, 1.35:1, and 1.28:1, respectively. The calcination was carried out in a box furnace under an air atmosphere (N_2:O_2= 8:2), with a heating rate of 2°C/min, followed by heating at 900°C for 10 hours. Additionally, the Co-included LLO was synthesized using $Ni_{0.163}Co_{0.163}Mn_{0.675}(OH)_2$ and Li_2CO_3 precursors at a 1.5:1 ratio, under the same conditions as the Co-free LLO.

Electrode Fabrication and Electrochemical measurements

To prepare the cathode slurry, the active material, Super C65, and polyvinylidene fluoride (PVDF) were mixed in a weight ratio of 80:10:10. The prepared slurry was cast onto Al foil with loading densities of approximately 4 mg cm^{-2} and 11 mg cm^{-2}, followed by drying in a convection oven at 120 °C for 20 minutes. Subsequently, the electrode was pressed to achieve an active material density of 2.5 g cm^{-3}. For electrochemical property assessment, CR2032 coin cells were assembled, utilizing an electrolyte composed of 1.3M $LiPF_6$ in ethylene carbonate (EC): diethyl carbonate (DEC) = 3:7 (v/v) with 10 wt% fluoroethylene carbonate (FEC) additive.

All electrochemical tests were conducted at 45°C using a battery cycler (WonATech; WBCS3000Le32). Prior to electrochemical testing, each cell was rested for 10 hours to allow

electrolyte infiltration. For the low-loading samples, the activation cycle was conducted at a current density of C/30, with 1C defined as 250 mA g^{-1}. After activation, cycle retention tests were performed at a current density of C/3 (1C = 250 mA g^{-1}). For the high-loading samples, prepared for real application testing, the activation cycle was conducted at a current density of C/20 (1C = 250 mA g^{-1}), followed by cycle retention tests at C/2 (1C = 250 mA g^{-1}). All electrochemical tests were performed within a voltage window of 2.0 to 4.8 V (vs. Li/Li^+). The galvanostatic intermittent titration technique (GITT) protocol consisted of a current density pulse of C/30 for 10 minutes, followed by a 30-minute rest period for equilibration.

Materials Characterization.

To verify the size and morphology of the samples, scanning electron microscopy (SEM) was conducted using a HITACHI S-4800. The electron-transparent sample for transmission electron microscopy (TEM) was prepared using a focused ion beam (FIB, Helios NanoLab 450). High-angle annular dark field (HAADF) imaging of the domain structure and anti-site defects was conducted via scanning transmission electron microscopy (STEM, Neo ARM) using a spherical aberration correction system, operated at 200 kV. Synchrotron X-ray diffraction (sXRD) measurements were performed at the 9B HRPD beamline of the Pohang Accelerator Laboratory (PAL), Republic of Korea. The sXRD patterns were collected over a 2θ range of 15° to 135°, with a step size of 0.01° and an exposure time of 2 seconds. ND patterns were collected using the high-resolution powder diffractometer (HRPD) at the Korea Atomic Energy Research Institute (KAERI), operating at a fixed wavelength of 1.834544 Å. Data were recorded across a 2θ range from 0° to 160°, with an increment of 0.05° per step. Rietveld refinement was carried out using the FullProf program[1]. Hard X-ray absorption spectroscopy data were obtained from beamlines 6D C&S UNIST-PAL (XAFS) and 7D XAFS

at PAL, with Ni and Mn K-edge spectra measured in transmission mode at room temperature. All spectra were processed using the Athena program. Soft X-ray absorption spectroscopy was conducted at beamlines 4D PES and 10A2 HRPES II at PAL, with O K-edge and Mn L-edge spectra measured in total electron yield (TEY) mode at room temperature. The spectra were processed using the Beagle program. The magnetic properties of the powder samples were investigated using a SQUID magnetometer (MPMS-VSM, Quantum Design) at the Korea Basic Science Institute (KBSI). Magnetic moment measurements were performed in sweep mode across the temperature range from 300 K to 2 K, with the magnetic field fixed at 1500 Oe.

First-principles calculations

First-principles calculations based on Density Functional Theory (DFT) were conducted using the spin-polarized Generalized Gradient Approximation (GGA). The core electrons were represented through the Projector Augmented Wave (PAW) method, as implemented in the Vienna Ab initio Simulation Package (VASP)[2]. We employed the Perdew-Burke-Ernzerhof (PBE) exchange-correlation functional and utilized plane waves with a cut-off energy of 600 eV. Hubbard U corrections were set at 3.9 eV for Mn and 6.2 eV for Ni to accurately account for the electron-electron interactions in these transition metals[3]. The Brillouin zone for the DFT calculations was sampled using a 4*2*1 k-point mesh.

DFT calculations struggle to accurately predict strain terms. To better assess the energy penalty from anti-site defects, two models were employed. The first examined the trend in energy penalty by varying slab distance, while the second evaluated the penalty in a perfectly phase-aligned structure.

The energy penalty associated with the alignment of the $LiTMO_2$ (R phase) and Li_2MnO_3 (M phase) phases was calculated based on two model cases. i) To model the effect of anti-site defects, where the c lattice parameter of the R phase remains mostly unchanged but the TM and Li slab distances vary significantly, the energy penalty was calculated by adjusting only the slab distances, while keeping the c lattice of each phase fixed in its ground state. The slab distance was varied by adjusting the oxygen sites. ii) The energy penalty was evaluated under a distinct configuration where the lattice parameters and slab distances of both the $LiTMO_2$ and Li_2MnO_3 phases formed a fully coherent interface. In both cases, the positions of the oxygen atoms were relaxed along the a- and b-axes, while the c-axis was fixed to maintain slab distance alignment.

To assess the average bond strength of M-O (M = Mn_{TM}, Ni_{TM}, Ni_{Li}, Li_{Li}, Li_{TM}) bonds, the integrated crystal orbital Hamilton population (-ICOHP) values were computed using LOBSTER program[4, 5].

To evaluate whether anti-site defects influence the oxygen reactivity of M phase at the R-M interface, we modeled both defect-free ($Li_{12}Ni_6Mn_6O_{24}$ + $Li_{16}Mn_8O_{24}$) and Li-Ni anti-site defect ($[Li_{10}Ni_2][Li_2Ni_4Mn_6]O_{24}$ + $Li_{16}Mn_8O_{24}$) systems.

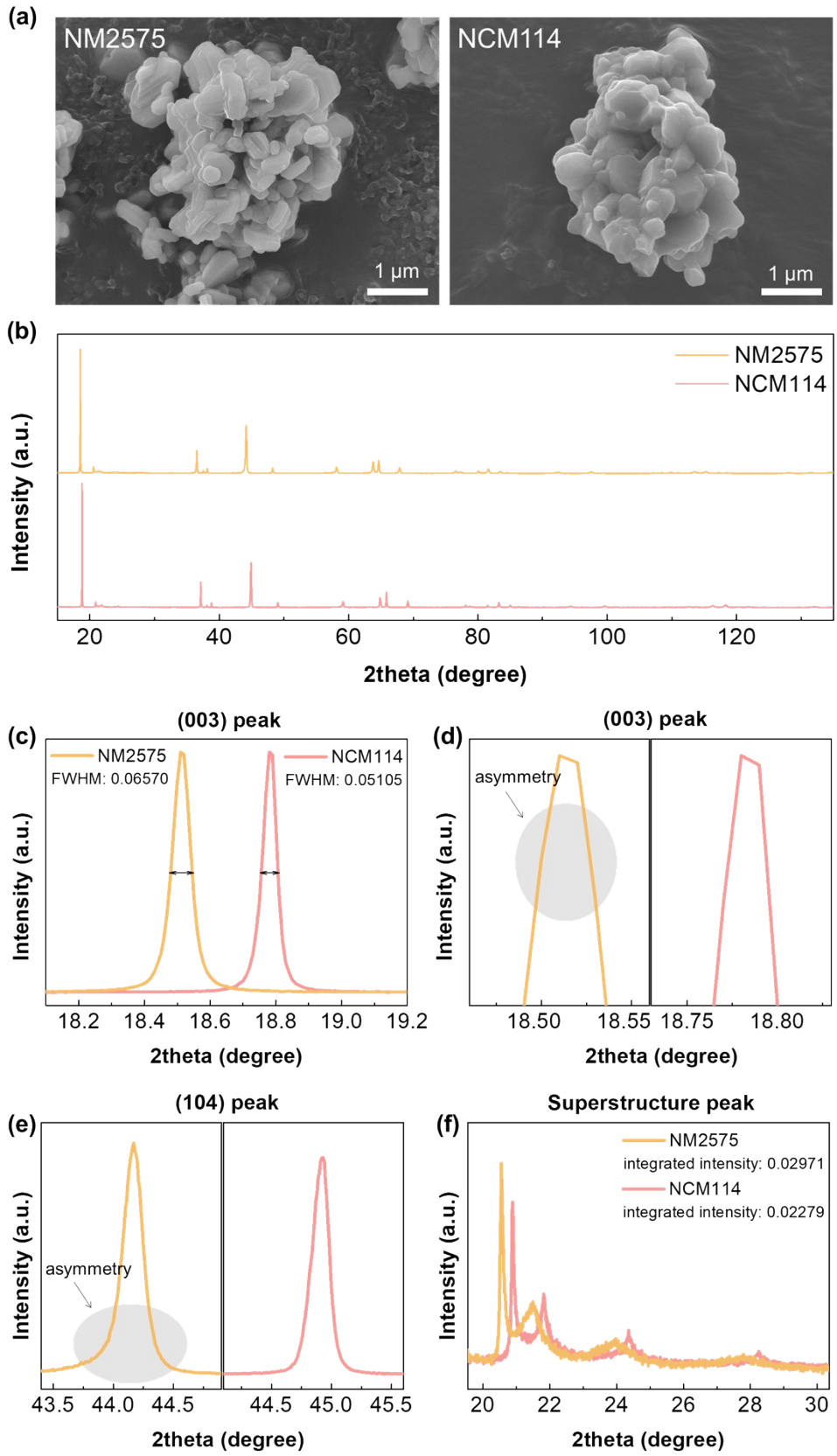
(a)
NM2575
1 μm
NCM114
1 μm
(b)
NM2575
NCM114
Intensity (a.u.)
20
40
60
80
100
120
2theta (degree)
(c)
(003) peak
NM2575
FWHM: 0.06570
NCM114
FWHM: 0.05105
Intensity (a.u.)
18.2
18.4
18.6
18.8
19.0
19.2
2theta (degree)
(d)
(003) peak
asymmetry
Intensity (a.u.)
18.50
18.55
18.75
18.80
2theta (degree)
(e)
(104) peak
asymmetry
Intensity (a.u.)
43.5
44.0
44.5
44.5
45.0
45.5
2theta (degree)
(f)
Superstructure peak
NM2575
integrated intensity: 0.02971
NCM114
integrated intensity: 0.02279
Intensity (a.u.)
20
22
24
26
28
30
2theta (degree)

Supplementary Fig. 1. Degree of homogeneity of R-M phase in Co-free LLO and Co-included LLO.

(a) Morphology of secondary particles of $Li_{1.2}Ni_{0.2}Mn_{0.6}O_2$ (Ni:Mn=25:75, hereafter NM2575) and Co-included $Li_{1.2}Ni_{0.13}Co_{0.13}Mn_{0.54}O_2$ (Ni:Co:Mn=1:1:4, hereafter NCM114) **(b)** Whole sXRD patterns of $Li_{1.2}Ni_{0.2}Mn_{0.6}O_2$ (Ni:Mn=25:75, hereafter NM2575) and Co-included $Li_{1.2}Ni_{0.13}Co_{0.13}Mn_{0.54}O_2$ (Ni:Co:Mn=1:1:4, hereafter NCM114) **(c)** Full width at half maximum (FWHM) of (003) peak in NM2575 and NCM114. **(d)** Asymmetricity of (003) peak in NM2575 and NCM114. **(e)** Asymmetricity of (104) peak in NM2575 and NCM114. **(f)** Integrated intensity of superstructure peak in NM2575 and NCM114.

Supplementary Text for Supplementary Fig. 1.

As the rhombohedral phase (R phase) and monoclinic phase (M phase) share all peak positions except for the superstructure peaks observed between 20˚ and 30˚, the broadness of the peaks provides insights into the extent of phase integration between the R and M phases[4]. The (003) peak, which is the most representative peak for layered materials, in layered oxides provides information about the *c*-axis. In Li-rich layered oxide LLO materials, the (003) peak of the R phase and the (001) peak of the M phase merge to form a single peak. Therefore, in general, the broadness or asymmetry of this peak is considered an important measure of the coherence between the two phases[5]. We confirmed the XRD pattern of the prepared Li-rich layered powders using synchrotron high-resolution XRD (sXRD), which utilizes monochromatic incident X-rays to minimize peak asymmetry originating from the equipment. Therefore, the asymmetry observed in the sXRD pattern is attributed solely to the characteristics of the samples. The whole XRD patterns for both Co-free and Co-included LLO are shown in **Fig. S1(b)**. In the case of Co-free $Li_{1.2}Ni_{0.2}Mn_{0.6}O_2$ (Ni:Mn=25:75, hereafter NM2575), a broader (003) peak is observed (**Fig. S1(c)**), along with noticeable asymmetry. Notably, a greater level of asymmetry is observed in the gray-colored region of NM2575 (**Fig. S1(d)**). Additionally, the (104) peak, another representative peak of the layered material,

exhibits greater asymmetry in NM2575, as indicated by the gray-shaded region (**Fig. S1(e)**). On the other hand, Co-included $Li_{1.2}Ni_{0.13}Co_{0.13}Mn_{0.54}O_2$ (Ni:Co:Mn=1:1:4, hereafter NCM114) exhibits a sharper (003) and (104) peaks and, notably, a symmetric peak shape in the peak region, indicating good lattice coherency. Additionally, the integrated intensity of the superstructure peak allows for the evaluation of the crystallinity of the M phase. Despite having the same R-M phase fraction for both samples, the Co-free NM2575 exhibits an integrated intensity of the superstructure peak approximately 30% larger. This discrepancy suggests that NM2575 exhibits relatively poor R-M phase integrity and the formation of larger domains (**Fig. S1(f)**).

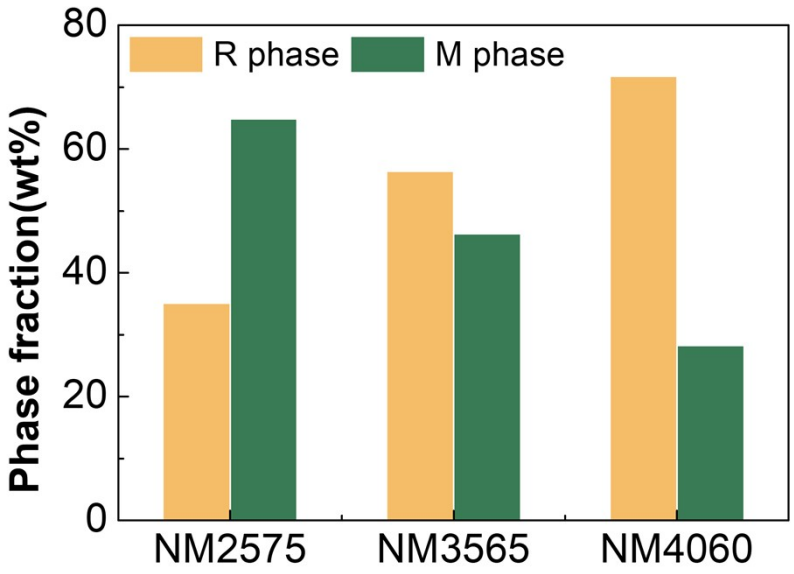

Supplementary Fig. 2. Phase fraction of Co-free LLOs derived from Rietveld refinement of neutron diffraction.

Supplementary Text for Supplementary Fig. 2.

Here, we utilized Li-sensitive neutron diffraction to distinguish between the two phases and conducted Rietveld refinement. Due to the crystallographic similarity between the two phases within LLO, it is challenging to perfectly distinguish the phase fractions. However, we confirmed that the fraction of the R phase increases as the overall Ni content increases, indicating these samples remain suitable for a systematic series study.

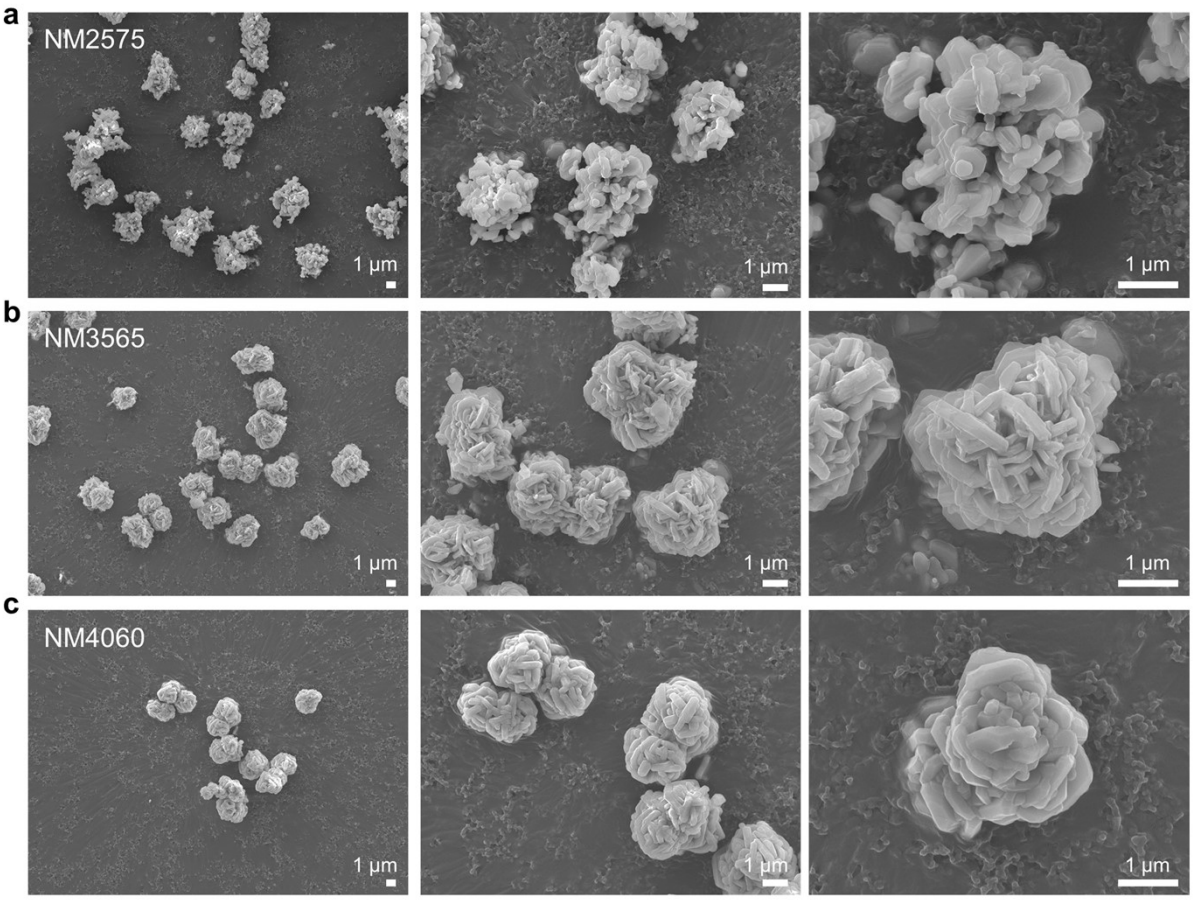

Supplementary Fig. 3. Morphology of secondary particles depending on TM ratio in Co-free LLOs.

(a) $Li_{1.2}Ni_{0.2}Mn_{0.6}O_2$ (Ni:Mn=25:75, NM2575) (**b)** $Li_{1.13}Ni_{0.304}Mn_{0.565}O_2$ (Ni:Mn=35:65, NM3565) (**c)** $Li_{1.091}Ni_{0.364}Mn_{0.545}O_2$ (Ni:Mn=40:60, NM4060)

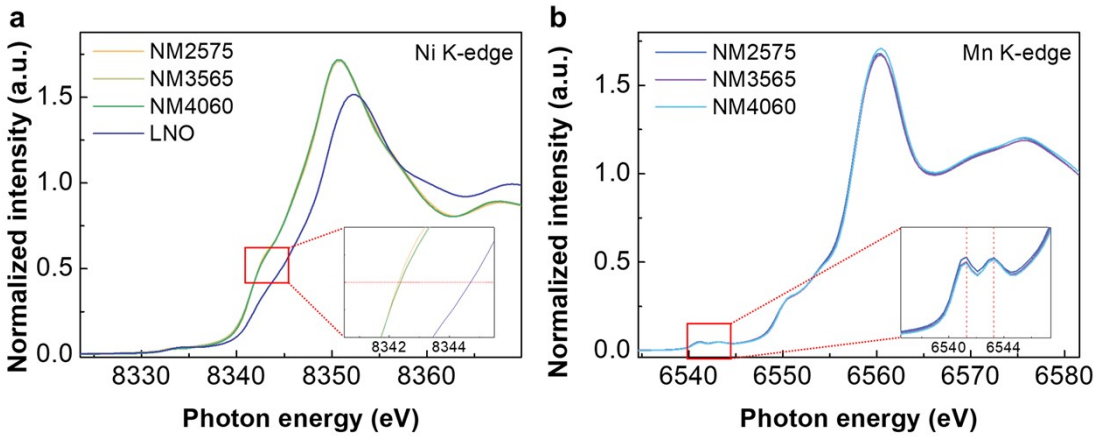

Supplementary Fig. 4. Valence state of Ni and Mn in Co free-LLOs.

(a) XANES spectra of Ni K-edge in Co-free LLOs. (**b)** XANES spectra of Mn K-edge in Co-free LLOs.

Supplementary Text for Supplementary Fig. 4.

Examination of the Ni K-edge XANES region reveals that all Co-free Li-rich layered oxides (LLOs) exhibit a normalized intensity of approximately 0.5 at the same photon energy, indicating a consistent valence state across these materials. Furthermore, inspection of the pre-edge region of the Mn K-edge shows no photon energy shift, confirming an identical valence state across all samples.

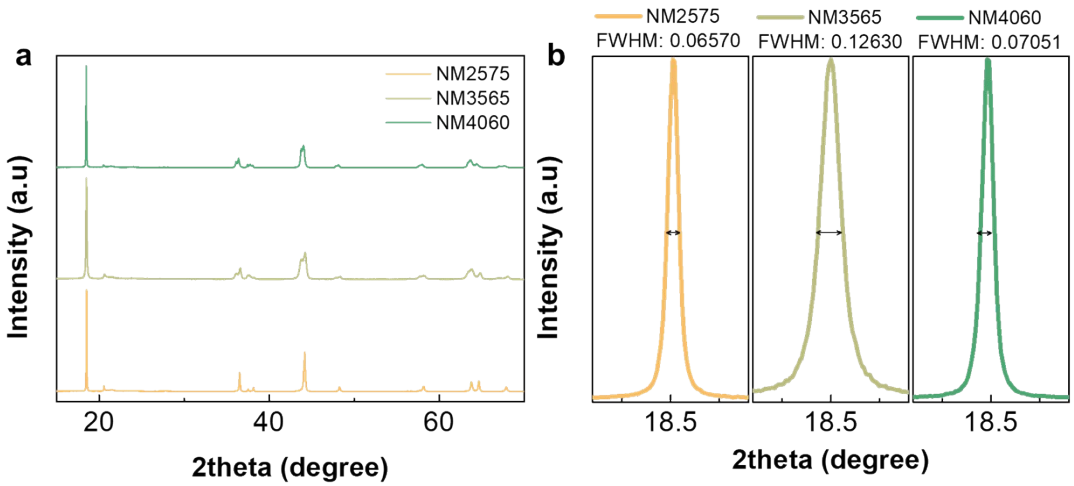

Supplementary Fig. 5. XRD patterns of Co-free LLOs and FWHM of (003) in Co-free LLOs.

Supplementary Text for Supplementary Fig. 5.

The (003) peaks of NM3565 and NM4060 exhibit significant broadness, resembling the bifurcation trend observed in the (104) peak. This suggests poor lattice coherency between the R and M phases along the c-axis. It is worth noting that no peaks corresponding to the spinel phase were observed in this two-theta region. Additionally, TEM observations (**Fig. S7**) did not reveal the presence of any other phases, such as spinel or rock salt. Therefore, we can conclude that the bifurcation or changes in the (003) peak observed here are attributed exclusively to R-M phase segregation.

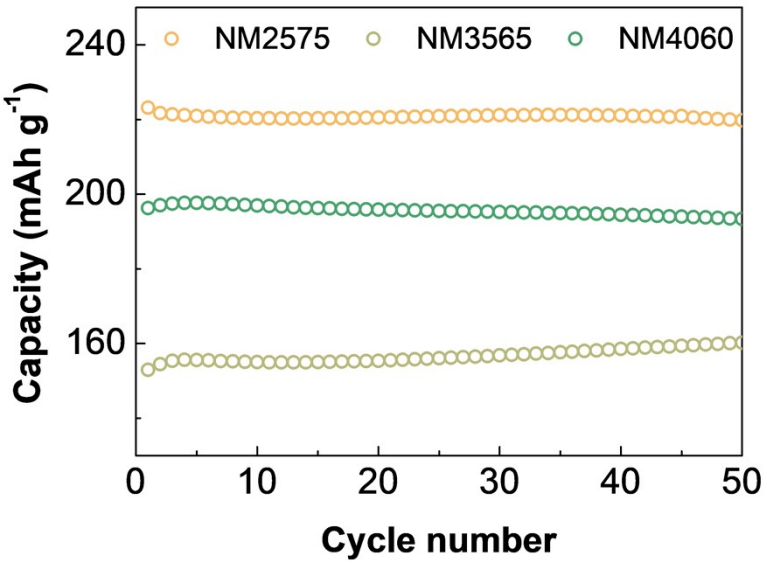

Supplementary Fig. 6. Cycle life of Co-free LLOs.

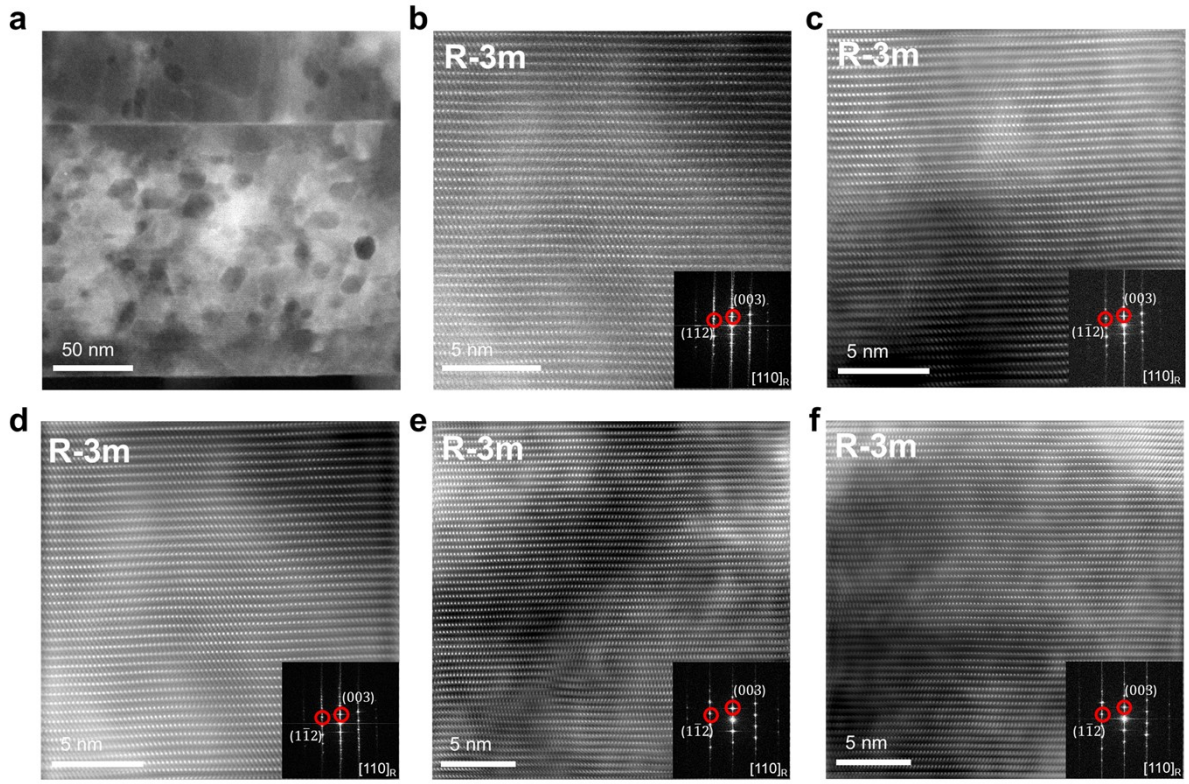

Supplementary Fig. 7. The severe phase segregation in the NM3565 sample.

(a) Primary particle of NM3565. **(b)-(f)** phase segregated R phase region.

Supplementary Text for Supplementary Fig. 7.

Fig. S7(a) depicts a TEM image of primary particles of NM3565. **Fig. S7(b)-S7(f)**, taken from this region, all show R-phase regions exclusively observed along the $[110]_R$ zone axis, confirming the highly phase-segregated nature of the sample.

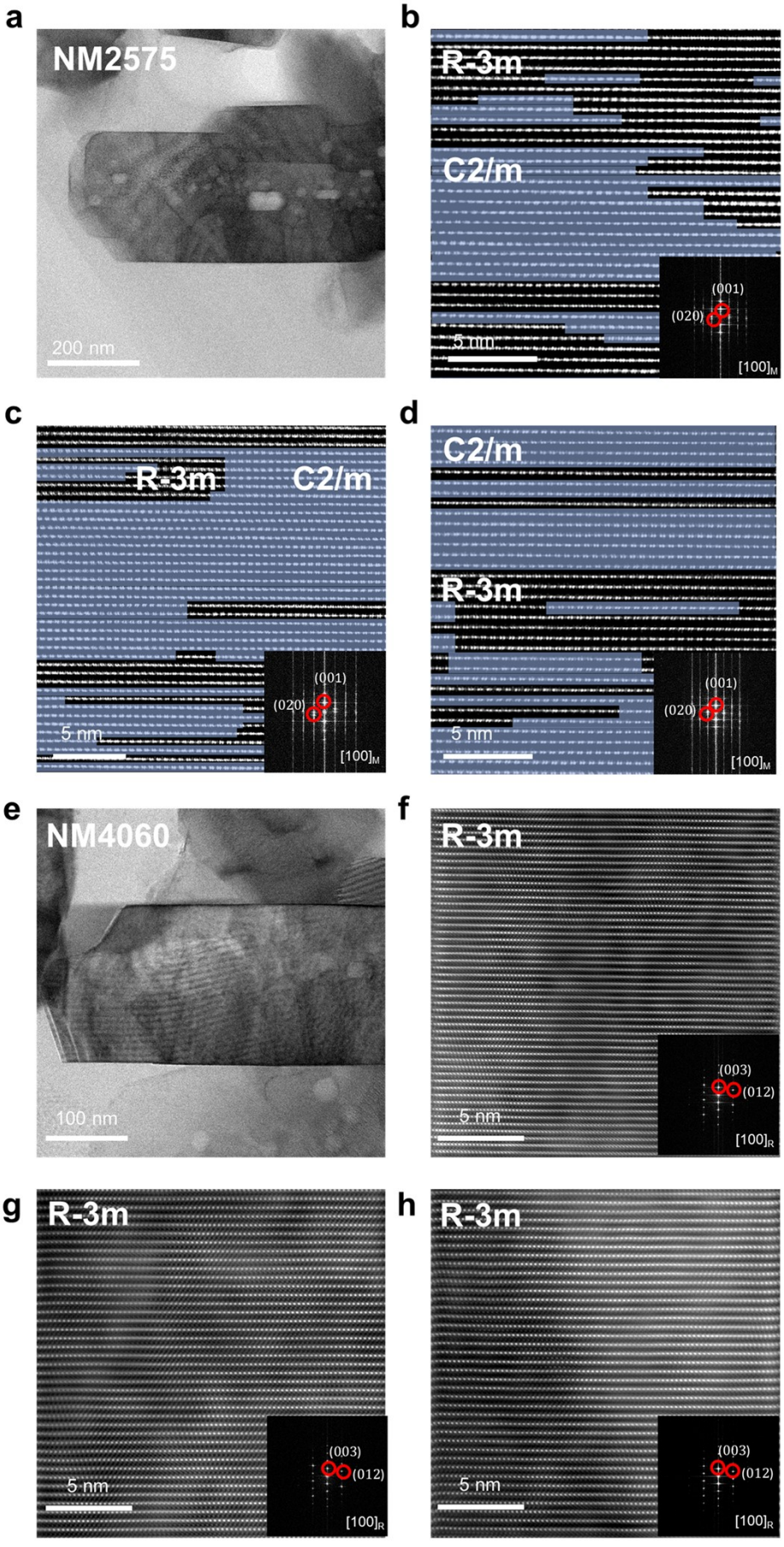
a
NM2575
200 nm
b
R-3m
C2/m
(001)
(020)
5 nm
[100]M
c
R-3m
C2/m
(001)
(020)
5 nm
[100]M
d
C2/m
R-3m
(001)
(020)
5 nm
[100]M
e
NM4060
100 nm
f
R-3m
(003)
(012)
5 nm
[100]R
g
R-3m
(003)
(012)
5 nm
[100]R
h
R-3m
(003)
(012)
5 nm
[100]R

Supplementary Fig. 8. The domain distribution in the NM2575 and NM4060 sample.

(a) Primary particle of NM2575. **(b)-(d)** Distribution of R and M phase domain in NM2575. **(e)** Primary particle of NM4060. **(f)-(h)** phase segregated R phase region of NM4060.

Supplementary Text for Supplementary Fig. 8

Fig. S8(a) and **S8(e)** present TEM images of the primary particles of NM2575 and NM4060, respectively. **Fig. S8(b)-S8(d)** and **Fig. S8(f)-S(h)** were captured from these primary particles. NM4060, which shows peak splitting in the XRD pattern along with NM3565, exhibits clear segregation of the R phase domains within the primary particles. In contrast, NM2575, which demonstrates higher phase integrity in the XRD pattern compared to other Co-free LLOs, shows a more homogeneous distribution of R and M phases within the primary particles.

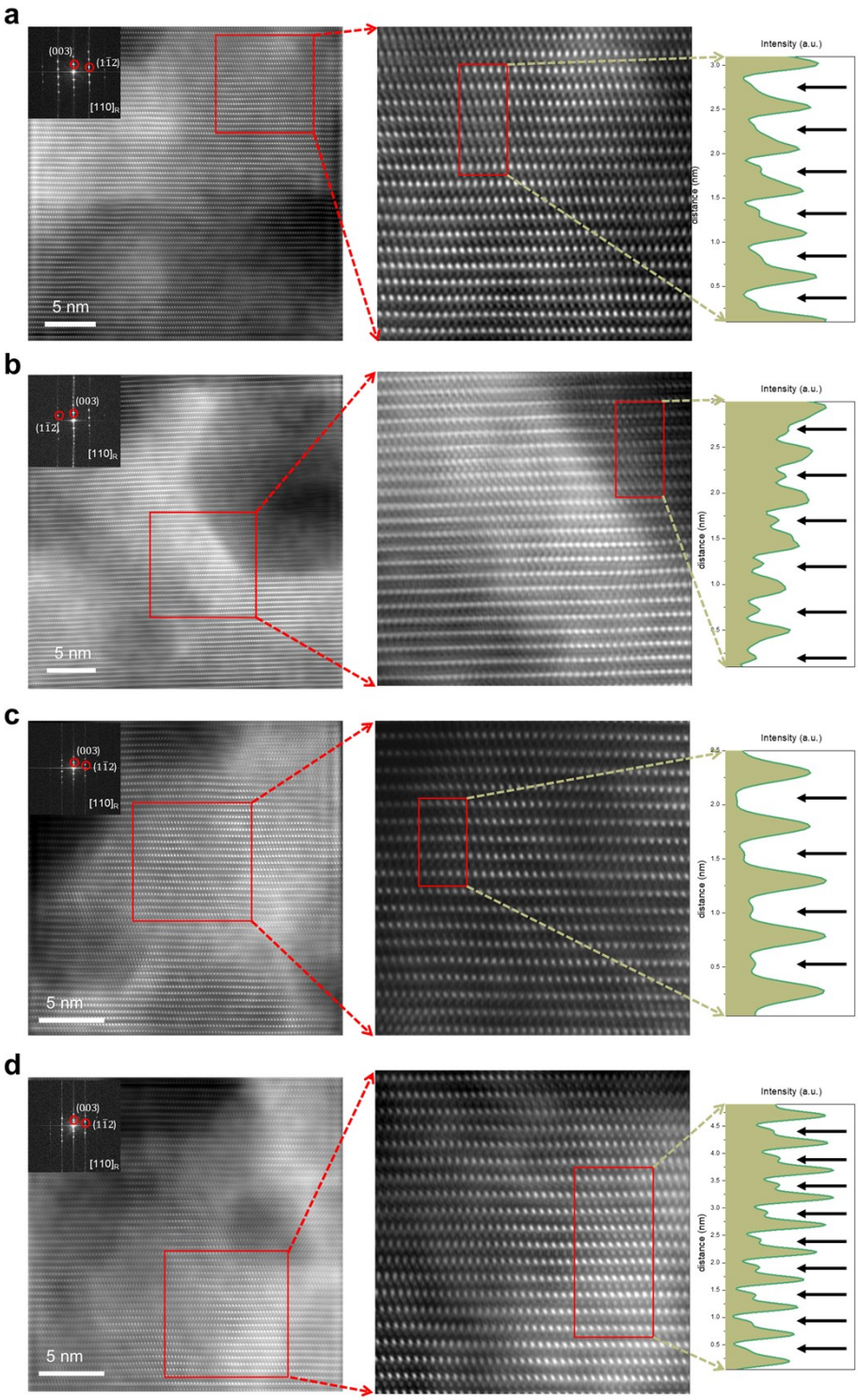

Supplementary Fig. 9. Observation of Ni_{Li} anti-site defects in NM3565 sample. The red box indicates the presence of Ni_{Li} anti-site defects.

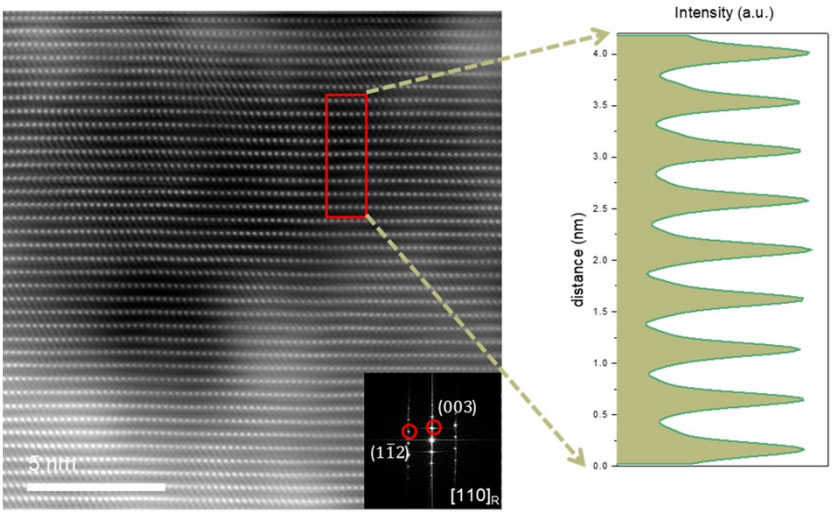

Supplementary Fig. 10. The normal layered region without anti-ste defects of R phase in NM3565. This region is part of Supplementary Fig. 7.

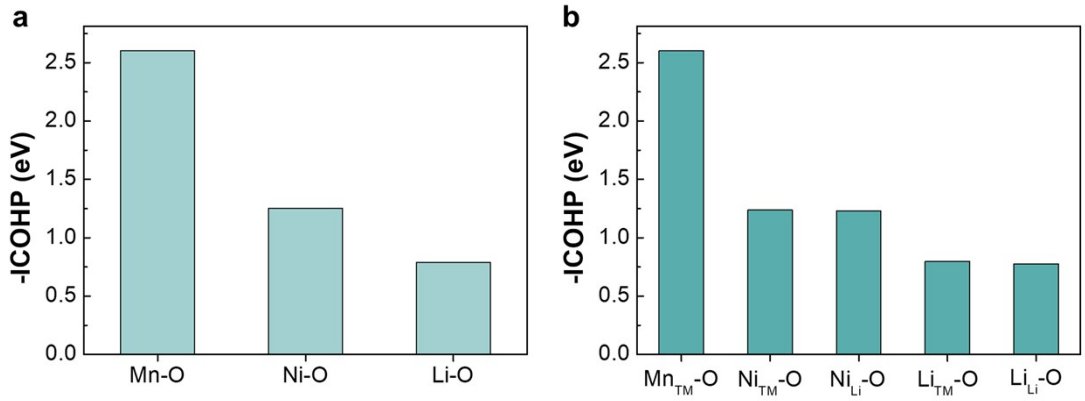

Supplementary Fig. 11. M-O bond strength depending on the presence of anti-site defects **(a)** bond strength of defect-free system, (**b)** bond strength of system with anti-site defects

Supplementary Text for Supplementary Fig. 11.

Previous studies have reported that in layered oxide systems, TM-O bond strength is generally higher than Li-O bond strength. To further verify this, we examined bond strength in two systems: $LiNi_{0.5}Mn_{0.5}O_2$ (defect-free system) and $(Li_{0.84}Ni_{0.16})(Li_{0.16}Ni_{0.34}Mn_{0.5})O_2$ (system with anti-site defects).

Using integrated crystal orbital Hamilton population (ICOHP) analysis, we theoretically evaluated the bond strength in each system. In the defect-free structure, the TM-O bond strength is stronger than the Li-O bond strength. Similarly, in the defective structure, TM-O bonds remain stronger than Li-O bonds, regardless of the site occupied by the exchanged atoms.

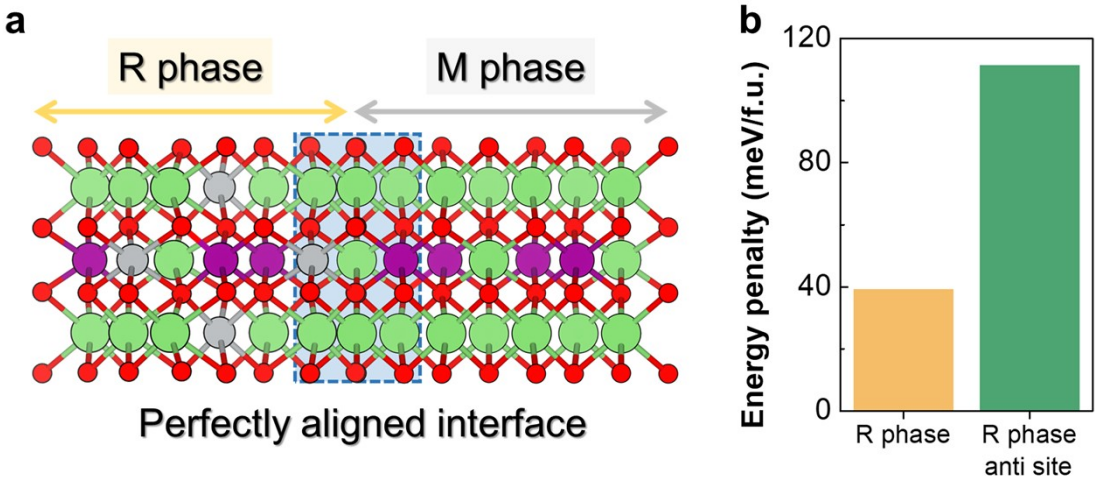

Supplementary Fig. 12. Energy penalty experienced by the R phase in a perfectly coherent R-M interface.

(a) Scheme of a perfectly aligned interface between the R and M phases. **(b)** Energy penalty from adjusting the lattice parameter and slab distance of the R phase to match the M phase (relative to the energy of the relaxed R phase).

Supplementary Text for Supplementary Fig. 12.

Since DFT calculations have limitations in accurately predicting strain, we double-checked the strain using two different models. First, we examined the trend of energy penalty changes with varying slab distances (**Fig. 2(f)**). Second, we assessed the energy penalty arising from the specific configuration where the R and M phases form a perfectly phase-aligned structure. Although precise strain modeling is challenging, through these two model studies, we confirmed that the mixing energy penalty between the two phases increases due to anti-site defects.

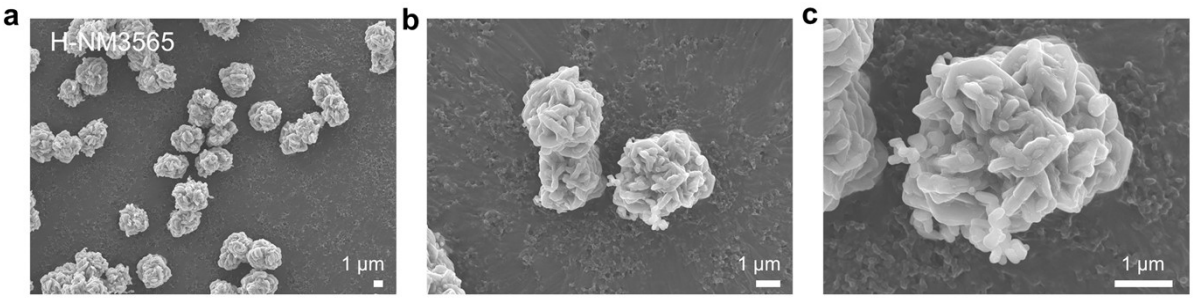

Supplementary Fig. 13. Morphology of secondary particles in $Li_{1.149}Ni_{0.298}Mn_{0.553}O_2$ (hereafter, Li/TM=1.35, H-NM3565, 'H' means homogenous domain distribution).

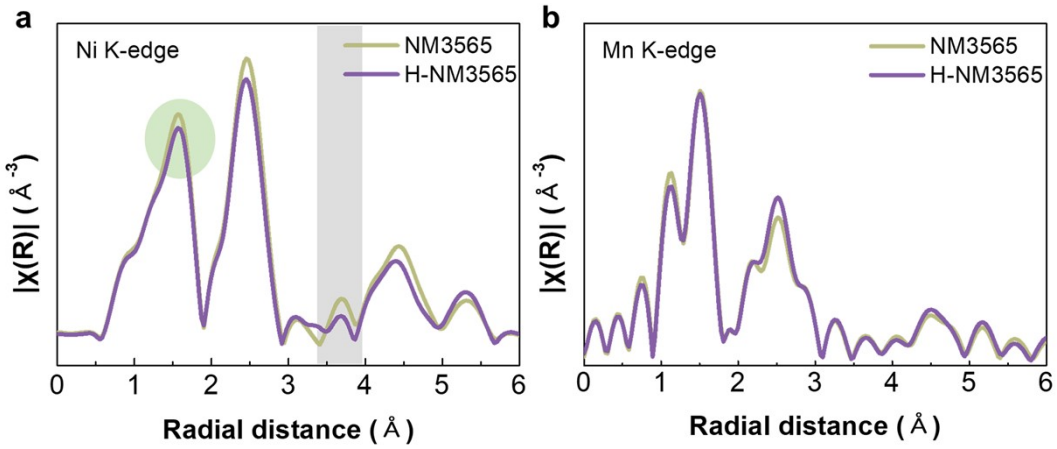

Supplementary Fig. 14. The Ni and Mn K-edge EXAFS profiles of NM3565 and H-NM3565.

Supplementary Text for Supplementary Fig. 14.

Through the peaks attributed to the Ni-O bond in the Ni K-edge EXAFS region, it is evident that the Ni valence state in H-NM3565 has increased slightly. The Ni^{3+} ion induces a soft Jahn-Teller effect, resulting in distortion of the oxygen ligands surrounding Ni. This distortion leads to variations in the Ni-O bond lengths, causing the first neighbor peak to broaden.

In each TM K-edge EXAFS spectrum, the first peak corresponds to the TM-O coordination signal from the first neighbor oxygen atoms, while the second peak corresponds to the TM-TM coordination signal from the second neighbor transition metal atoms. The higher Ni-TM intensity indicates that TM occupies more sites as the second neighbor of Ni, compared to Li, which is undetectable via X-ray scattering. This indicates that the M phase, where Li exists within the TM slab, is less prevalent around the R phase. This suggests that the R phase in NM3565 is segregated. Conversely, the lower Mn-TM intensity in NM3565 than in H-

NM3565 suggests an abundance of Li in the second neighbor sites of Mn in NM3565, indicating segregation within the M phase.

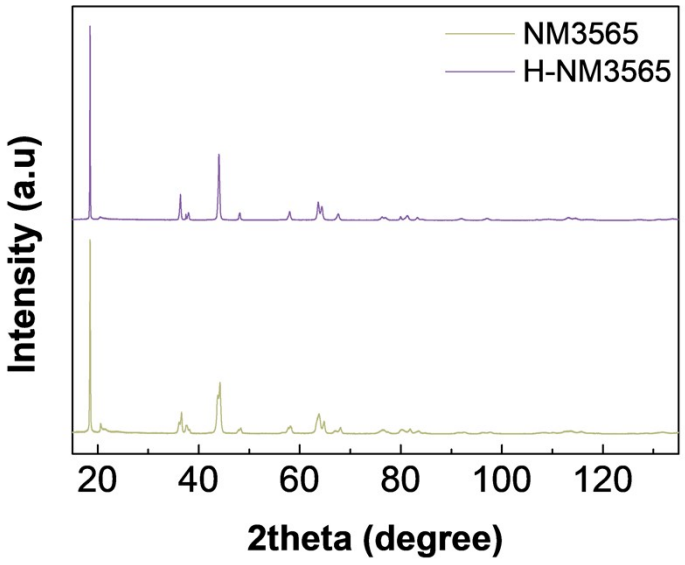

Supplementary Fig. 15. Full range of sXRD pattern in NM3565 and H-NM3565.

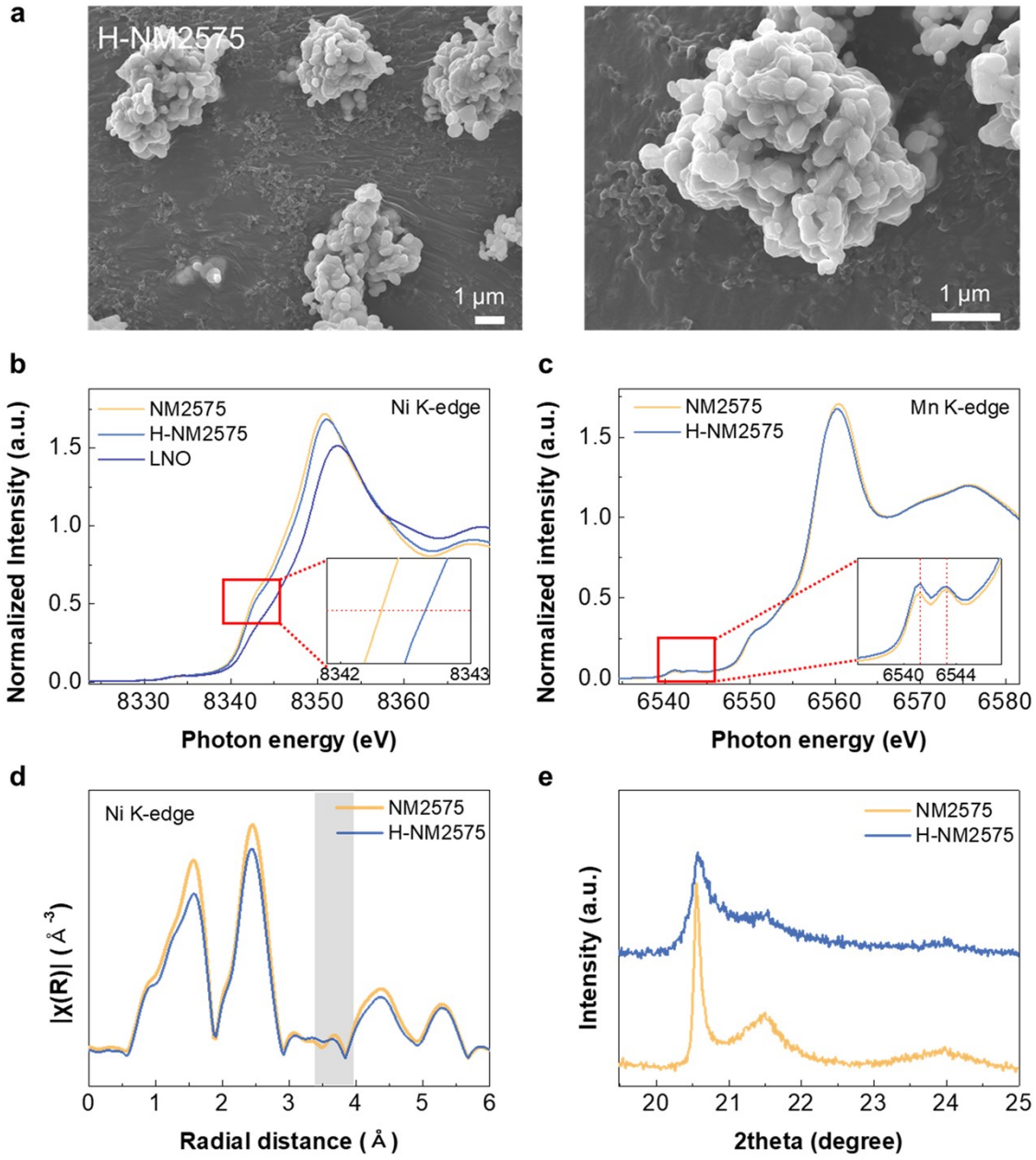

Supplementary Fig. 16. Off-stoichiometric composition of NM2575, $Li_{1.225}Ni_{0.194}Mn_{0.581}O_2$ (hereafter, Li/TM=1.58, H-NM2575).

(a) Morphology of H-NM2575. **(b)** Ni K-edge of NM2575 and H-NM2575. **(c)** Ni K-edge of NM2575 and H-NM2575. **(d)** Ni K-edge EXAFS profile of NM2575 and H-NM2575. **(e)** XRD pattern with superstructure peak of NM2575 and H-NM2575.

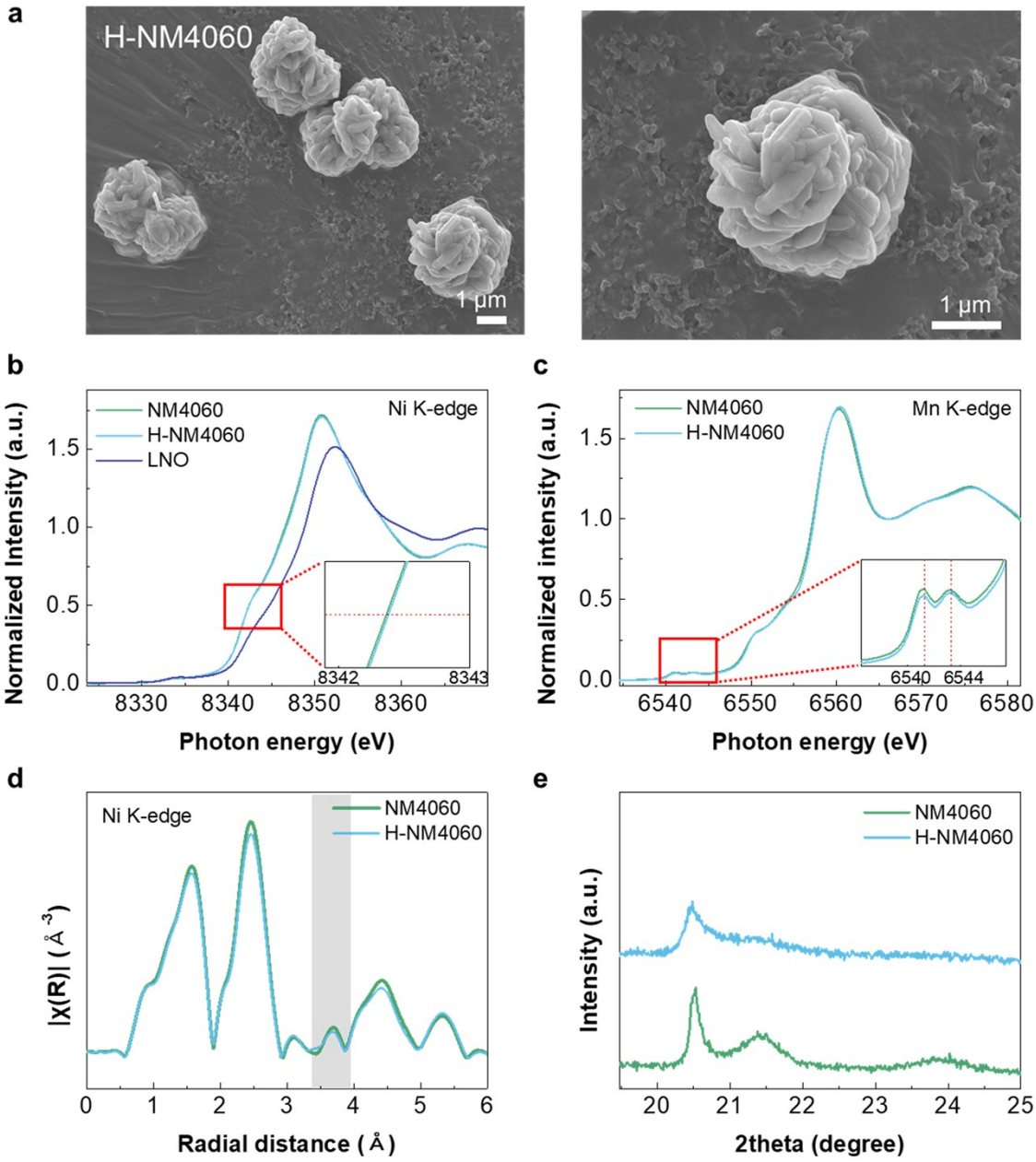

Supplementary Fig. 17. Off-stoichiometric composition of NM4060, $Li_{1.123}Ni_{0.351}Mn_{0.526}O_2$ (hereafter, Li/TM=1.28, H-NM4060).

(a) Morphology of H-NM4060. **(b)** Ni K-edge of NM4060 and H-NM4060. **(c)** Ni K-edge of NM4060 and H-NM4060 **(d)** Ni K-edge EXAFS profile of NM4060 and H-NM4060. **(e)** XRD pattern with superstructure peak of NM4060 and H-NM4060.

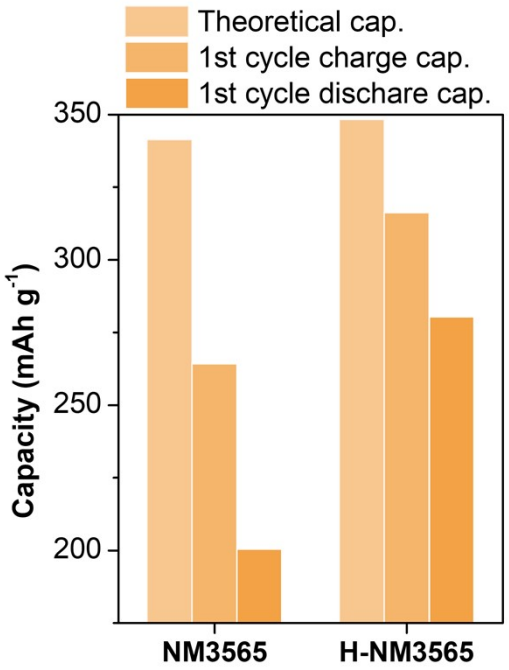

Supplementary Fig. 18. Comparison between the theoretical capacity and the first cycle charge-discharge capacity of NM3565 and H-NM3565.

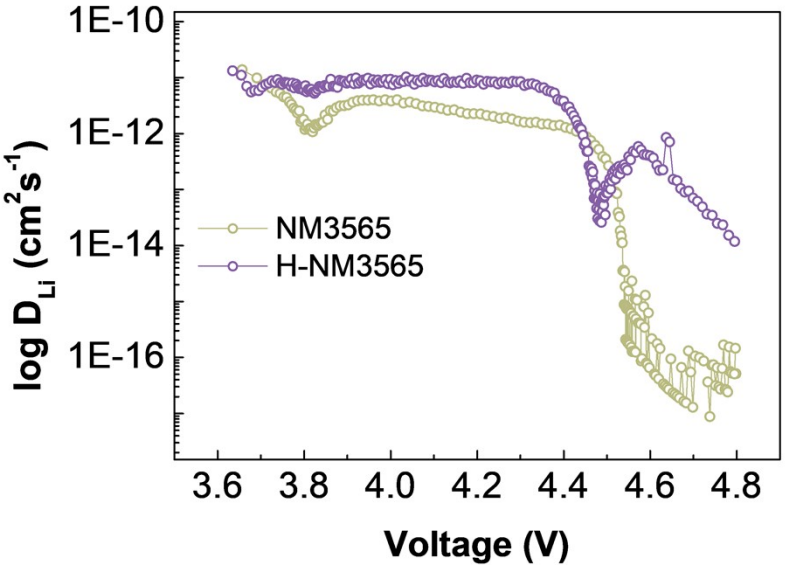

Supplementary Fig. 19. GITT profiles at 1st cycle during charge of NM3565 and H-NM3565.

Supplementary Text for Supplementary Fig. 19.

The galvanostatic intermittent titration technique (GITT) confirmed that the Li-ion diffusivity of H-NM3565 is much higher than that of NM3565 in the entire SoC region. Particularly in the region above 4.47V, where oxygen oxidation occurs, H-NM3565 demonstrates Li-ion diffusivity 3-4 orders of magnitude higher than NM3565, facilitating stable oxygen activation. Electrochemical activation occurring within the high voltage range involves pronounced structural rearrangement along with lattice oxygen release.

NM3565 exhibits an electrolyte decomposition signal above 4.7V, as shown in **Fig. 5(a)**. This signal is attributed to the reaction between singlet oxygen, formed during the evolution of surface lattice oxygen, and the electrolyte, indicating poor surface oxygen stability in NM3565. Furthermore, the release of oxygen leads to an increase in irreversible capacity, resulting in a low ICE of approximately 75.9% for NM3565. In contrast, H-NM3565 exhibits an ICE of approximately 87.61%, and the absence of an electrolyte decomposition signal suggests a relatively improved surface oxygen stability.

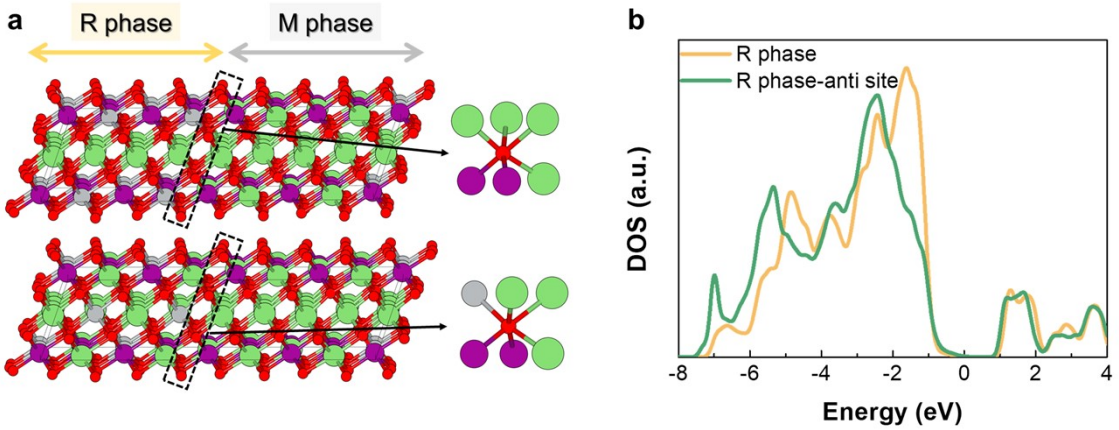

Supplementary Fig. 20. Influence of anti-site defects on oxygen redox activity at R-M interface.

(a) R-M interface models without (top) and with (bottom) anti-site defects, along with their corresponding local atomic configurations in the M phase. Dashed boxes denote oxygen atoms present at the R-M interface. **(b)** O2*p* projected density of states for each configuration of R phase.

Supplementary Text for Supplementary Fig. 20.

We further modeled the R-M interface to investigate the oxygen reactivity influenced by anti-site defects (**Fig. S20(a)**). The oxygen activity was evaluated through the projected density of states (pDOS) of oxygen atoms located at the interface in both the defect-free and defect-included models. Our results show that the pDOS of the defect-free model is shifted towards higher energy levels compared to the defect-included model, indicating higher oxygen reactivity at the defect-free interface (**Fig. S20(b)**). This suggests that H-NM3565, with a controlled defect concentration, exhibits enhanced oxygen reactivity.

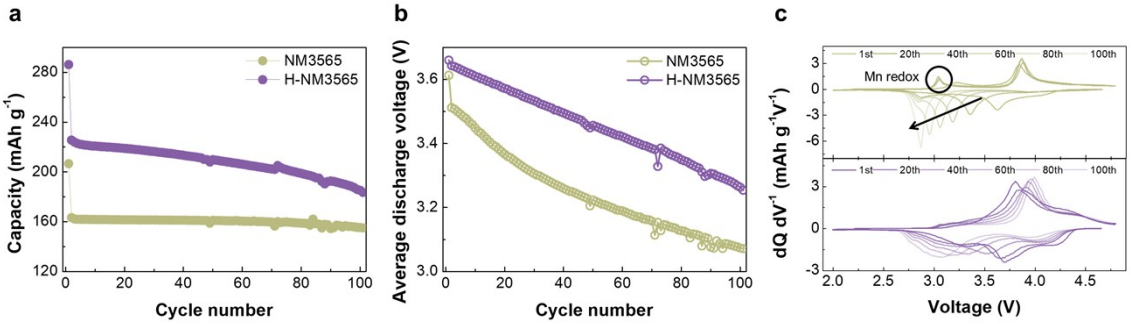

Supplementary Fig. 21. The long cyclability performance for real application conditions.

(a) Cycle life graph of NM3565 and H-NM3565. **(b)** Average discharge voltage graph of NM3565 and H-NM3565. **(c)** dQ dV^{-1} profile of NM3565 and H-NM3565 during cycling.

Supplementary Text for Supplementary Fig. 21.

As observed in the low-loading experiments, NM3565 fails to fully activate the oxygen redox even under high loading conditions, whereas H-NM3565 achieves sufficient activation, resulting in over 50 mAh g^{-1} higher capacity in subsequent cycles. As cycling progresses, NM3565 undergoes significant structural degradation, leading to pronounced voltage decay and reduced electrochemical reversibility. H-NM3565 also experiences capacity decline due to increased oxygen participation in the redox process at elevated temperatures. Nevertheless, H-NM3565 consistently delivers higher energy density than NM3565 under realistic application conditions.

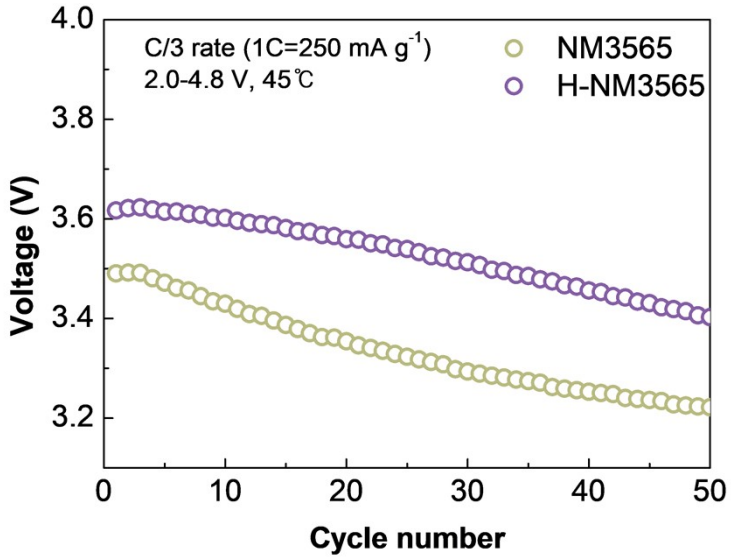

Supplementary Fig. 22. Average discharge voltage graph of NM3565 and H-NM3565

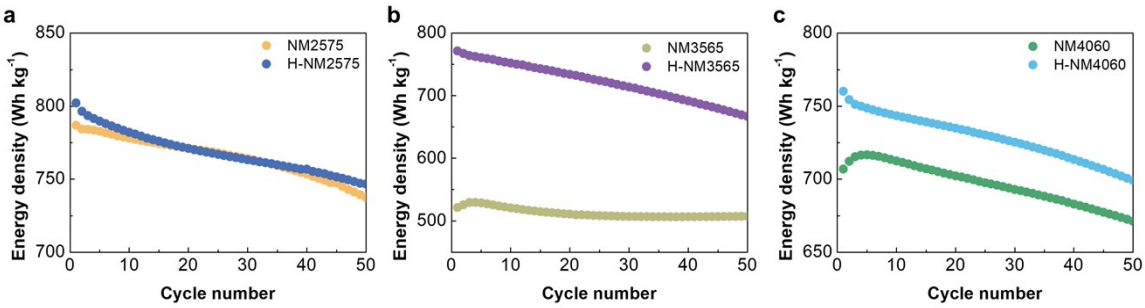

Supplementary Fig. 23. Energy density of Co-free NM compositions and off-stoichiometric Co-free NM compositions

(a) Energy density profile of NM2575 and H-NM2575, **(b)** Energy density profile of NM3565 and H-NM3565, **(c)** Energy density profile of NM4060 and H-NM4060

Supplementary Tables

LNO					
atom	**x**	**y**	**z**	**B**	**Occupancy**
Li	0	0	0	1.3	0.978 (2)
Ni	0	0	0	1.3	0.022 (2)
Li	0	0	0	0.511	0.022 (2)
Ni	0	0	0	0.511	0.978 (2)
O	0	0	0.2421 (1)	1.023	2.000

LNO	
a (Å)	2.87650 (1)
b (Å)	2.87650 (1)
c (Å)	14.19719 (9)
Vol (Å3)	101.733 (0)
Rwp	8.36
Chi2	4.78
Cation mixing	2.2

Supplementary Table 1. Results of Rietveld refinement of $LiNiO_2$

NM2575_R phase					
atom	**x**	**y**	**z**	**B (fix)**	**Occupancy**
Li	0	0	0.5	1.3	0.937 (8)
Ni	0	0	0.5	1.3	0.062 (8)
Li	0	0	0	0.5	0.062 (8)
Ni	0	0	0	0.5	0.437 (8)
Mn	0	0	0	0.5	0.500
O	0	0	0.257 (1)	0.7	2.000

NM2575_M phase					
atom	**x**	**y**	**z**	**B (fix)**	**Occupancy**
Li	0	0.64 (2)	0.5	1.3	0.5
Li	0	0	0.5	1.3	0.25
Li	0	0.5	0	1.3	0.25
Mn	0	0.169 (2)	0	0.5	0.5
O	0.25 (1)	0.329 (6)	0.21 (1)	0.7	1
O	0.228 (2)	0	0.23 (1)	0.7	0.5

NM2575	**R phase**	**M phase**
a (Å)	2.86062 (8)	4.9598 (7)
b (Å)	2.86062 (8)	8.575 (1)
c (Å)	14.2660 (6)	5.0405 (6)
beta (°)	-	109.49 (1)
Vol (Å3)	101.101 (1)	202.089 (9)
TM slab distance (Å)	2.1640	2.0850
Rwp	15.5	
Chi2	4.82	
Cation mixing	6.2	-

Supplementary Table 2. Results of Rietveld refinement of NM2575

NM3565_R phase					
atom	**x**	**y**	**z**	**B (fix)**	**Occupancy**
Li	0	0	0.5	1.3	0.885 (6)
Ni	0	0	0.5	1.3	0.115 (6)
Li	0	0	0	0.5	0.115 (6)
Ni	0	0	0	0.5	0.385 (6)
Mn	0	0	0	0.5	0.500
O	0	0	0.256(1)	0.7	2.000

NM3565_M phase					
atom	**x**	**y**	**z**	**B (fix)**	**Occupancy**
Li	0	0.67 (1)	0.5	1.3	0.5
Li	0	0	0.5	1.3	0.25
Li	0	0.5	0	1.3	0.25
Mn	0	0.167 (1)	0	0.5	0.5
O	0.264 (6)	0.329 (3)	0.212 (4)	0.7	1
O	0.236 (8)	0	0.210 (5)	0.7	0.5

NM3565	**R phase**	**M phase**
a (Å)	2.8885 (3)	4.9421 (7)
b (Å)	2.8885 (3)	8.5604 (1)
c (Å)	14.283 (1)	5.0313 (4)
beta (°)	-	109.00 (1)
Vol (Å3)	103.206 (4)	201.25 (1)
TM slab distance (Å)	2.2009	2.0178
Rwp	13.2	
Chi2	3.61	
Cation mixing	11.5	-

Supplementary Table 3. Results of Rietveld refinement of NM3565

NM4060_R phase					
atom	**x**	**y**	**z**	**B (fix)**	**Occupancy**
Li	0	0	0.5	1.3	0.906 (4)
Ni	0	0	0.5	1.3	0.094 (4)
Li	0	0	0	0.5	0.094 (4)
Ni	0	0	0	0.5	0.406 (4)
Mn	0	0	0	0.5	0.500
O	0	0	0.2579 (7)	0.7	2.000

NM4060_M phase					
atom	**x**	**y**	**z**	**B (fix)**	**Occupancy**
Li	0	0.65 (1)	0.5	1.3	0.5
Li	0	0	0.5	1.3	0.25
Li	0	0.5	0	1.3	0.25
Mn	0	0.168 (1)	0	0.5	0.5
O	0.277 (7)	0.329 (4)	0.216 (8)	0.7	1
O	0.24 (1)	0	0.22 (1)	0.7	0.5

NM4060	**R phase**	**M phase**
a (Å)	2.8821 (1)	4.9606 (9)
b (Å)	2.8821 (1)	8.606 (1)
c (Å)	14.2909 (9)	5.039 (8)
beta (°)	-	109.16 (2)
Vol (Å3)	102.805 (3)	203.23 (1)
TM slab distance (Å)	2.2097	2.0594
Rwp	14.2	
Chi2	4.50	
Cation mixing	9.4	-

Supplementary Table 4. Results of Rietveld refinement of NM4060

M phase	
a (Å)	4.99588
b (Å)	8.63543
c (Å)	5.07212
β (θ)	109.5536
TM slab distance (Å)	2.1608
Li slab distance (Å)	2.6188
Relative E (meV/f.u.)	-
R phase	
a (Å)	5.05895
b (Å)	8.81874
c (Å)	5.08310
β (θ)	109.0840
TM slab distance (Å)	2.1833
Li slab distance (Å)	2.6204
Relative E (meV/f.u.)	0
R phase-anti	
a (Å)	5.02350
b (Å)	8.86785
c (Å)	5.06097
β (θ)	108.3646
TM slab distance (Å)	2.2097
Li slab distance (Å)	2.5936
Relative E (meV/f.u.)	64.2

Supplementary Table 5. Results of relaxed structure in DFT calculations

H-NM3565_R phase					
atom	**x**	**y**	**z**	**B (fix)**	**Occupancy**
Li	0	0	0.5	1.3	0.922 (3)
Ni	0	0	0.5	1.3	0.078 (3)
Li	0	0	0	0.5	0.078 (3)
Ni	0	0	0	0.5	0.459 (3)
Mn	0	0	0	0.5	0.462
O	0	0	0.2579 (6)	0.7	2.000

H-NM3565_M phase					
atom	**x**	**y**	**z**	**B (fix)**	**Occupancy**
Li	0	0.65 (1)	0.5	1.3	0.5
Li	0	0	0.5	1.3	0.25
Li	0	0.5	0	1.3	0.25
Mn	0	0.166 (1)	0	0.5	0.5
O	0.248 (7)	0.327 (4)	0.222 (9)	0.7	1
O	0.22 (1)	0	0.22 (1)	0.7	0.5

H-NM3565	**R phase**	**M phase**
a (Å)	2.87285 (6)	4.9489 (7)
b (Å)	2.87285 (6)	8.705 (1)
c (Å)	14.2789 (7)	5.0330 (8)
beta (°)	-	108.95 (1)
Vol (Å3)	102.060 (2)	205.07 (1)
Rwp	12.6	
Chi2	3.52	
Cation mixing	7.8	-

Supplementary Table 6. Results of Rietveld refinement of H-NM3565

REFERENCE

1. R. Carvajal and J. Fullprof, 1990.
2. G. Kresse and J. Hafner, *Journal of Physics: Condensed Matter*, 1994, **6**, 8245.
3. B. Himmetoglu, A. Floris, S. De Gironcoli and M. Cococcioni, *International Journal of Quantum Chemistry*, 2014, **114**, 14-49.
4. R. Dronskowski and P. E. Bloechl, *The Journal of Physical Chemistry*, 1993, **97**, 8617-8624.
5. S. Maintz, V. L. Deringer, A. L. Tchougréeff and R. Dronskowski, *J. Comput. Chem.*, 2013, **34**, 2557-2567.
6. J. Hwang, S. Myeong, W. Jin, H. Jang, G. Nam, M. Yoon, S. H. Kim, S. H. Joo, S. K. Kwak and M. G. Kim, *Adv. Mater.*, 2020, **32**, 2001944.
7. T. Ungar, *Scripta Materialia*, 2004, **51**, 777-781.